The Astrophysical Journal Letters, 880:L19 (5pp), 2019 August 1 https://doi.org/10.3847/2041-8213/ab2ed9

A Luminous Molecular Gas Pair beyond Redshift 7

Ekaterina Koptelova and Chorng-Yuan Hwang
Graduate Institute of Astronomy, National Central University, Taoyuan City 32001, Taiwan; koptelova@astro.ncu.edu.tw
Received 2019 March 26; revised 2019 July 1; accepted 2019 July 3; published 2019 July 26

Abstract

We report the first detection of molecular gas beyond redshift 7. The molecular gas is associated with the host galaxy of the quasar candidate PSO J145.5964+19.3565 and its companion PSO J145.5964+19.3565N separated by 20.7 kpc. The molecular gas of both companions is detected in two rotational transition lines of carbon monoxide, CO(6–5) and CO(7–6), with total luminosities of $L_{\rm CO(6-5)} \approx 26 \times 10^8$ and $L_{\rm CO(7-6)} \approx 17 \times 10^8\,L_\odot$. The two companions contain (36–54) $\times\ 10^{10}\,M_\odot$ of molecular gas assuming that their CO spectral line energy distributions are typical for star-forming galaxies. We also detected the Lyα line of PSO J145.5964+19.3565 at $z \approx 7.08$. The Lyα line emission is extended and might represent the blended emission of two different sources at a separation of <5 kpc. The detected CO and Lyα emission likely originate from a system of interacting star-forming galaxies that might host a quasar(s). We also report the detection of a new emission line from the system that is a possible 793.62-GHz water maser line.

Key words: cosmology: observations – galaxies: general – galaxies: high-redshift – galaxies: ISM

1. Introduction

Molecular gas may constitute a significant fraction of the total mass of high-redshift star-forming galaxies and host galaxies of high-redshift quasars (Bertoldi et al. 2003; Walter et al. 2003; Genzel et al. 2010; Bothwell et al. 2013; Venemans et al. 2017a). The physical properties of molecular gas provide important insights on the formation of massive galaxies and their coevolution with supermassive black holes.

Carbon monoxide (hereafter CO) is the most common tracer of molecular gas (composed mainly of molecular hydrogen, H_2; Solomon & Vanden Bout 2005; Carilli & Walter 2013). The current most distant detections of molecular gas using CO line emission are from the host galaxies of luminous high-redshift quasars and massive star-forming galaxies at $6 < z < 6.9$ (Bertoldi et al. 2003; Walter et al. 2003; Wang et al. 2010, 2011a, 2011b; Riechers et al. 2013; Strandet et al. 2017; Venemans et al. 2017a). These galaxies are among the largest reservoirs of molecular gas known at high redshift.

The total mass and distribution of molecular gas is well traced by the CO line emission in ground-state transition CO(1–0) (Young & Scoville 1991; Solomon & Vanden Bout 2005). However, this transition is difficult to observe from high-redshift sources (e.g., Riechers et al. 2006). At high redshift, the CO($J \sim 4$–8) transitions near the peak of the CO spectral line energy distribution (SLED) of star-forming galaxies become important tracers of molecular gas (Weiß et al. 2005, 2007; Riechers et al. 2009, 2011; Wang et al. 2010, 2011a, 2011b; Venemans et al. 2017a). These CO transitions can potentially be used to search for new high-redshift star-forming galaxies and quasars, especially for those that are optically faint, in the obscured phases of their formation (e.g., Vieira et al. 2013; Weiß et al. 2013; Strandet et al. 2016; Fudamoto et al. 2017).

In this Letter, we report the discovery of a luminous molecular gas pair at $z = 7.09$ using the CO(6–5) and CO(7–6) line observations of $z > 6.5$ quasar candidates selected from the Panoramic Survey Telescope and Rapid Response System 1 survey (PS1; Chambers et al. 2016). The detected CO emission is associated with the quasar candidate PSO J145.5964+19.3565 (hereafter PSO145+19). The CO redshift of PSO145+19 was confirmed by the detection of the UV Lyα λ1216 line at the similar redshift.

2. Observations

2.1. ALMA Observations

PSO145+19 was observed in Band 3 of the Atacama Large Millimeter/submillimeter Array (ALMA) on 2016 August 20 and 30. The observations were carried out in frequency intervals ~84–92 and 96–104 GHz to observe the CO(6–5) and CO(7–6) transitions ($\nu_{\rm rest} = 691.47$ and 806.65 GHz) from quasar candidates at $6.5 \lesssim z \lesssim 7.2$ selected using the following criteria: $z_{\rm PS1} - y_{\rm PS1} > 2$, photometric error $\sigma_{y_{\rm PS1}} < 0.1$, and $z_{\rm PS1} < 24$ AB magnitudes (Koptelova et al. 2017).

The synthesized beam sizes (spatial resolution) of the data obtained on 2016 August 20 and 30 were $\sim 0\farcs9 \times 0\farcs7$ and $0\farcs7 \times 0\farcs4$, respectively. The total on-source time at each epoch was about 19 minutes. The visibility data were imaged using task CLEAN of the Common Astronomy Software Applications (CASA 4.7.0; McMullin et al. 2007) with a cell of $0\farcs12$, natural weighting and channel width of 23.44 MHz (~80 and 70 km s^{-1} in the lower and upper receiver sidebands, respectively). We run CLEAN with a taper parameter of $1''$ to reduce noise fluctuations. To identify emission lines, we created intensity maps by sequentially averaging five nearby frequency channels of data cubes. Each map covered ~400 km s^{-1}, which is the typical width of the CO lines detected from the host galaxies of high-redshift quasars (Wang et al. 2010). The maps were calculated using CASA task IMMOMENTS with MOMENTS $= -1$. We checked the maps for emission peaks with signal-to-noise ratios (S/Ns) > 3 at the expected frequency range of either CO(6–5) or CO(7–6). We then searched for the corresponding emission line regardless of the S/N of the latter.

2.2. Near-infrared Observations

The near-infrared spectrum of PSO145+19 (4×950 s exposures) was obtained using the Gemini Multi-Object

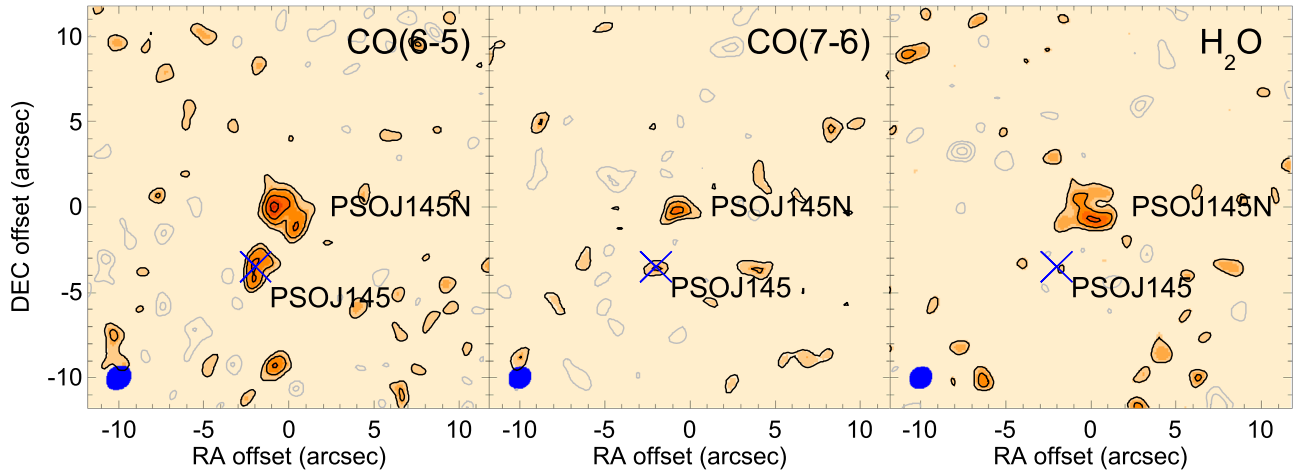

Figure 1. CO(6–5), CO(7–6), and H_2O intensity maps of PSO145+19 and PSO145+19N. The maps were calculated by averaging the 23.44-MGz channels within velocity ranges of ∼880, 910, and 550 km s^{-1}, respectively. The position of PSO145+19 measured by PS1 is marked with a cross. The beam size of the CO(6–5) map is $1\farcs4 \times 1\farcs1$ (7.1 × 5.6 kpc), and the beam size of the CO(7–6) and H_2O maps is $1\farcs2 \times 1\farcs0$ (6.1 × 5.2 kpc) (ellipses). Contours are drawn at (−3, −2, 2, 3, 4, 5) × σ, where $\sigma \approx 0.2$ mJy beam^{-1}. Negative contours are shown using gray lines.

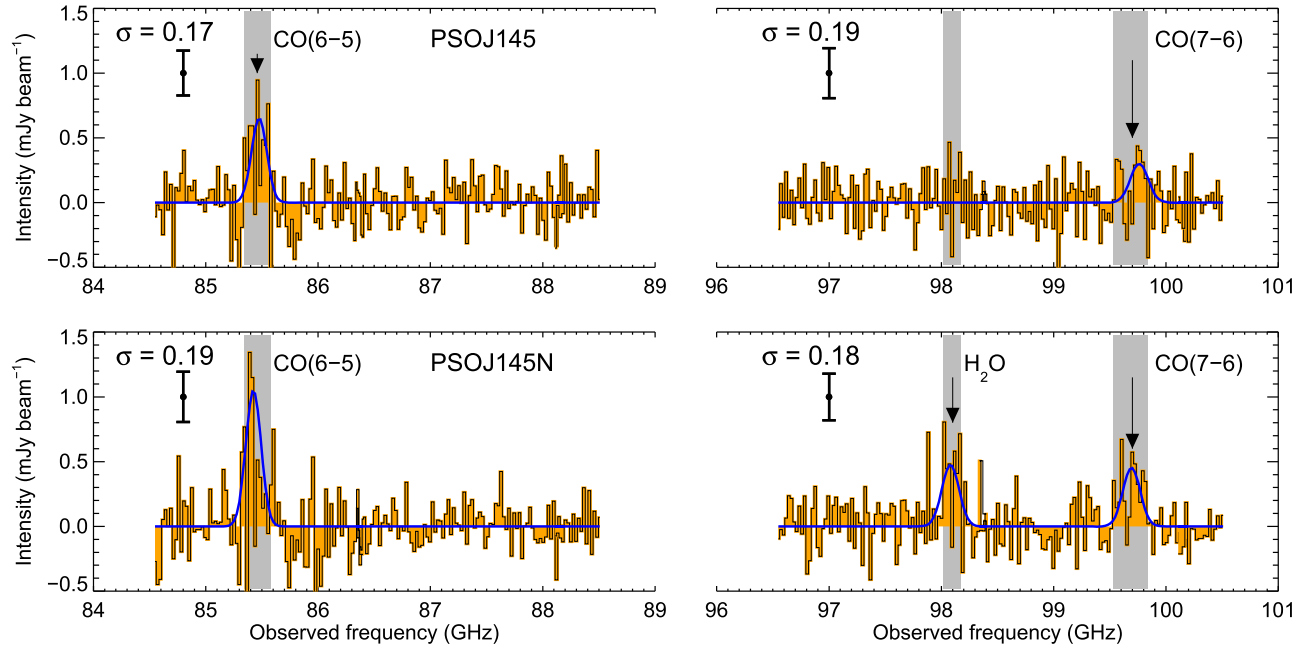

Figure 2. ALMA spectra of PSO145+19 and PSO145+19N binned to a resolution of 23.44 MHz. The Gaussian profiles of the lines are shown in blue. The shaded regions mark channels used for the calculation of the intensity maps. Error bars represent the typical rms errors.

Spectrograph (GMOS; Hook et al. 2004) of the Gemini North Telescope on 2017 October 28 under seeing of ∼0.″7. We used grating *R*400 and a slit width of 1″. The spatial resolution and dispersion of the data were 0.″1614 pixel^{-1} and 3.034 Å pixel^{-1}; the spectral resolution was $R \approx 960$. The flux calibration of the spectrum was performed using the GMOS spectrum of the standard star EG131 taken at a similar epoch. We also took deep *J*-band images of PSO145+19 with the UH2.2 telescope of the University of Hawaii on 2017 March 16 and 18 (see Section 3.2).

3. Results

3.1. CO and Water Emission Lines

In the 400 km s^{-1} intensity maps, we identified the CO(6–5) and CO(7–6) lines at a fixed frequency separation. The emission in both transitions is spatially extended and shows two luminous peaks (Figure 1). The fainter peak coincides with the PS1 position of PSO145+19, whereas the brighter peak, denoted PSO145+19N, is located 4″ away. The spectra of PSO145+19 and PSO145+19N presented in Figure 2 were extracted from the cleaned data cubes by integrating the intensities within apertures of 4″ in diameters centered on the two peaks. The aperture size was chosen so as to include more than 90% of the emission of PSO145+19N. The observed line profiles were fitted with Gaussians. The integrated S/Ns of the CO(6–5) and CO(7–6) lines, estimated using spectral channels within the Gaussian ±2σ of the lines, are about 10 and 5 for PSO145+19, and about 12 and 7 for PSO145+19N. Thus, even the CO(7–6) lines of PSO145+19 and PSO145+19N are not too significant at the line peaks ($S/N_{peak} \sim 2$ and 3, respectively), the integrated line S/Ns indicate that all detected

Table 1
Properties of the CO and Lyα Emission of PSO145+19 and PSO145+19N

Parameter	PSO J145+19	PSO J145+19N
R.A. (hh:mm:ss.ss)	09:42:23.14	09:42:23.00
decl. (dd:mm:ss.ss)	19:21:23.55	19:21:27.02
$z_{\rm CO}$	7.092 ± 0.006	7.093 ± 0.004
$z_{\rm H_2O}$		7.092 ± 0.004
FWHM $_{\rm CO(6-5)}$ (km s^{-1})	565 ± 90	589 ± 79
FWHM $_{\rm CO(7-6)}$ (km s^{-1})	565 ± 120	547 ± 98
FWHM$_{\rm H_2O}$ (km s^{-1})		551 ± 86
$I_{\rm CO(6-5)}$ (Jy km s^{-1})	2.81 ± 0.36	3.12 ± 0.40
$I_{\rm CO(7-6)}$ (Jy km s^{-1})	1.52 ± 0.38	1.80 ± 0.35
$I_{\rm H_2O}$ (Jy km s^{-1})		1.96 ± 0.36
$L_{\rm CO(6-5)}$ ($10^8\,L_\odot$)	12.3 ± 1.6	13.6 ± 1.7
$L'_{\rm CO(6-5)}$ (10^{10} K km s^{-1} pc^2)	11.6 ± 1.5	12.9 ± 1.7
$L_{\rm CO(7-6)}$ ($10^8\,L_\odot$)	7.7 ± 1.9	9.2 ± 1.8
$L'_{\rm CO(7-6)}$ (10^{10} K km s^{-1} pc^2)	4.6 ± 1.2	5.5 ± 1.1
$L_{\rm H_2O}$ ($10^8\,L_\odot$)		9.8 ± 1.8
$L'_{\rm H_2O}$ (10^{10} K km s^{-1} pc^2)		6.1 ± 1.1
$M_{\rm H_2}$ [a] ($10^{10}\,M_\odot$)	25.7 ± 2.9	29.1 ± 3.1
$M_{\rm H_2}$ [b] ($10^{10}\,M_\odot$)	16.2 ± 1.9	17.8 ± 1.9
Size (kpc)	8.2 ± 3.2	12.7 ± 1.6
$M_{\rm dyn}$ ($10^{10}\,M_\odot$)	36.6 ± 13.8	61.7 ± 7.8
$z_{{\rm Ly}\alpha,1}$	7.083 ± 0.003	
$z_{{\rm Ly}\alpha,2}$	7.086 ± 0.003	
FWHM$_{{\rm Ly}\alpha,1+2}$ (km s^{-1})	539 ± 36	
$L_{{\rm Ly}\alpha,1+2}$ (10^{43} erg s^{-1})	5.28 ± 0.22	

Notes.
[a] Assuming the CO SLED of SMM J16359+6612.
[b] Assuming the CO SLED of IRAS F10214+4724.

lines are quite significant and are not spurious detections. Moreover, the probability of a spurious detection of two emission lines at a fixed separation is extremely low. From the normal distribution, the probability of such a simultaneous event is on the order of 10^{-29}. Compared to these two lines, some other field detections seen in Figure 1 are not simultaneously detected in the CO(6–5) and CO(7–6) intensity maps and most likely represent random peaks.

The velocity-integrated fluxes of the lines, $I_{\rm line}$, were computed by summing the observed line intensities over spectral channels within $\pm 2\sigma$ of the lines as $I_{\rm line} = N_{\rm beam}\,\Delta\upsilon\Sigma_i I_i$, where I_i is the line intensity in channel i in Jy beam^{-1}, $\Delta\upsilon$ is the velocity width of the channel in km s^{-1}, and $N_{\rm beam}$ is the number of synthesized beams in the aperture. The flux uncertainties were calculated as $\sigma_{I_{\rm line}} = N_{\rm beam}\,\Delta\upsilon\sqrt{\Sigma_i \sigma_i^2}$, where σ_i is the rms error in channel i in mJy beam^{-1}. The luminosities of the emission lines were computed using formulae (1) and (3) of Solomon & Vanden Bout (2005).

The redshifts of PSO145+19 and PSO145+19N, measured as the mean redshifts of the CO(6–5) and CO(7–6) transitions, are similar within the uncertainties. The widths of the CO(6–5) and CO(7–6) lines were calculated as the Gaussian FWHM (see Table 1). The linear distance between PSO145+19 and PSO145+19N is 20.7 kpc (assuming a cosmology with $H_0 = 70$ km s^{-1} Mpc^{-1}, $\Omega_{\rm m} = 0.3$, and $\Omega_\Lambda = 0.7$). The emission from the dust continuum of PSO145+19 and PSO145+19N was not detected. The 3σ upper limit on the flux of the dust continuum estimated at the position of PSO145+19 is 0.99 mJy.

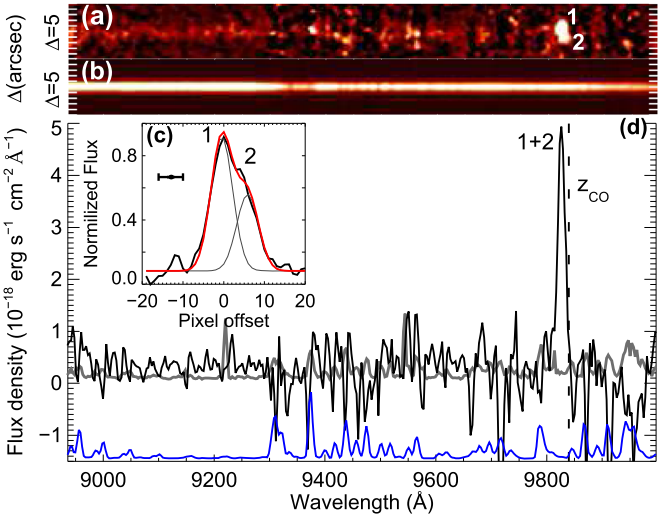

Figure 3. Lyα line emission of PSO145+19. The two-dimensional spectrum of PSO145+19 is shown in comparison with the spectrum of the field star (panels (a) and (b)). The observed spatial profile of the Lyα emission along the most extended direction is shown in panel (c) with a thick black line. The two Gaussians fitted into the spatial profile and their sum are shown with gray and red lines. The FWHM size of the field star is shown with an error bar. Panel (d) shows the total spectrum of 1 and 2. The error spectrum is shown by a thick gray line. The sky emission lines are shown in blue. The wavelength corresponding to the redshift of the CO emission of PSO145+19 is marked with a dashed line.

We also detected a third strong emission line in the spectrum of PSO145+19N with a line S/N of 5. This line is identified as a possible $H_2O(J_{K_aK_c} = 1_{10}$–$1_{01})$ water maser line at $\nu_{\rm rest} = 793.62$ GHz predicted by the calculations of Gray et al. (2016). According to Gray et al. (2016), the 793.62 GHz water emission originates from the dense and hot gas with densities of $n_{\rm H_2} > 10^6$ cm^{-3} and kinetic temperatures of $T_{\rm kin} \gtrsim 1000$ K. Compared to this water line, the CO emission traces less dense and colder gas with a density and temperature of $n_{\rm H_2} \sim 10^3$–10^5 cm^{-3} and $T_{\rm kin} \sim 100$ K (Weiß et al. 2005, 2007; Riechers et al. 2009, 2011).

To estimate the spatial extent of the CO emission of PSO145+19 and PSO145+19N, we fitted their CO(6–5) intensity distributions with two-dimensional Gaussians using CASA's task IMFIT. The characteristic sizes of these two CO companions were estimated as a quadratic mean of their FWHMs along the major and minor axes. We summarized the measured properties of the CO emission of PSO145+19 and PSO145+19N in Table 1.

3.2. Lyα Line

The Lyα emission line of PSO145+19 was detected at the wavelength interval that is not affected by sky emission lines. The line appears to be about two times more extended in the spatial direction compared to the spatial profile of a field star within 17″ of PSO145+19 observed simultaneously in the same slit. Thus, PSO145+19 might represent the blend of two Lyα lines from two different sources separated by less than 1″ (Figure 3(a)). At this separation the spectra of the sources are not fully resolved and their overlapping Lyα lines appear extended in the spatial direction. As shown in Figure 3(c), the spatial profile of the Lyα emission along its most extended direction can be described well by two blended Gaussians of the same widths equal to the FWHM of the field star.

Further, we denote the two Lyα peaks as sources 1 and 2. The total spectrum (extracted using an aperture of 12 pixels), which includes the Lyα emission of sources 1 and 2, is presented in Figure 3(d). The FWHM and luminosity of the Lyα line estimated from the Gaussian fit of the total spectrum are given in Table 1. The individual spectra of sources 1 and 2 were extracted using two adjacent apertures of 6 pixels in widths centered on each source. The redshifts of these two sources estimated from the Gaussian fit of their Lyα lines are $z = 7.083 \pm 0.003$ and 7.086 ± 0.003 with a small velocity offset of $\sim$120 km s^{-1}. The approximate FWHMs of the Lyα lines of 1 and 2 are $\sim$490 and 630 km s^{-1}. The Lyα lines of sources 1 and 2 are blueshifted with respect to the CO lines by about 340 and 210 km s^{-1}. Similar blueshifts of 100–3000 km s^{-1} of the UV emission lines relative to molecular and atomic lines have been observed in high-redshift quasars (Venemans et al. 2016; Mazzucchelli et al. 2017; Fan et al. 2018; Koptelova et al. 2019). The nearby UV continuum around the Lyα line emission was not detected, and therefore its estimated luminosity should be considered as a lower limit. The weak continuum is visible between sky emission residuals at wavelengths <9300 Å. The mean flux density of the continuum in region 9000–9300 Å, not contaminated by strong sky emission lines, is $(0.3 \pm 0.2) \times 10^{-18}$ erg s^{-1} cm^{-2} A^{-1} and its average S/N is $\sim$2. The detection of the UV continuum blueward of the Lyα line might indicate inhomogeneous reionization at redshift around 7 (e.g., Becker et al. 2015; Barnett et al. 2017).

The J-band brightness of PSO145+19 measured from the UH2.2 images is $m(J) = 21.87 \pm 0.17$ AB. There was no J-band source detected at the position of PSO145+19N. If PSO145+19N has a counterpart in the J band, it should be fainter than a 5σ limiting magnitude of 22.4 AB. Such faint sources are below the 5σ detection limit of PS1 in the $y_{\rm PS1}$ band (21 AB). To select PSO145+19, we used the first and second internal releases of the PS1 catalogs (see Koptelova et al. 2017). In these catalogs, the brightness of PSO145+19 measured from stack images is $m(y_{\rm PS1}) = 19.40 \pm 0.06$. However, we note that PSO145+19 was not detected by PS1 at almost all epochs except for one when its brightness was $m(y_{\rm PS1}) = 18.64 \pm 0.02$ AB[1] (2011 December 8). Only due to the contribution of this particular epoch into the $y_{\rm PS1}$-band stack flux of PSO145+19, it was selected by us as a high-redshift quasar candidate. One month later, PSO145+19 was also detected in the $z_{\rm PS1}$ band with $m(z_{\rm PS1}) = 18.72 \pm 0.04$ AB. The $z_{\rm PS1}$-/$y_{\rm PS1}$-band brightness of PSO145+19 at the epoch of our Gemini/GMOS observations, constrained from its total spectrum (Figure 3(d)), is $\gtrsim$24 AB magnitudes.

4. Discussion

The detected CO(6–5) and CO(7–6) line emission from the quasar candidate PSO145+19 revealed that it is associated with two luminous and extended molecular gas companions, PSO145+19 and PSO145+19N. Similar CO-luminous binary companions exhibit the host galaxies of some high-redshift quasars (e.g., Walter et al. 2004; Salomé et al. 2012).

The spatially extended Lyα line of PSO145+19 further suggests that it might represent a system of two sources at slightly different redshifts separated by <5 kpc (<1″). These two Lyα sources are not resolved in the CO line emission. The widths of the Lyα lines of PSO145+19 1 and 2 are consistent with those of some high-redshift star-forming galaxies and quasars (e.g., Matsuoka et al. 2018). The Lyα luminosity of PSO145+19, which is somewhat higher than the typical Lyα luminosities of star-forming galaxies ($\lesssim 10^{43}$ erg s^{-1}; Matsuoka et al. 2018), and evidence for variability of this source favor its interpretation as a quasar (or a quasar pair). The brightening of PSO145+19 detected in the $z_{\rm PS1}$ and $y_{\rm PS1}$ bands might be caused by significant variability of its continuum. Assuming that this variation is driven by a UV flare, we estimate an accretion disk size of $\log(R/{\rm cm}) = \log(ct) = 16.6$, where t is the PS1 cadence of 4 months in the rest frame of PSO145+19 adopted as the upper limit on the timescale of the observed variation. The inferred size is consistent with the UV sizes of the accretion disks of quasars estimated using microlensing (Blackburne et al. 2011). Thus, the two luminous CO companions (PSO145+19 and PSO145+19N) and the Lyα emission of PSO145+19 at the similar redshifts indicate that PSO145+19, initially selected as a single source quasar candidate, might represent a system of several interacting galaxies possibly hosting a quasar(s). The CO luminosity of the system indicates intensive star formation that might have been triggered by the interaction between the galaxies. The previous observations of the host galaxies of high-redshift quasars and submillimeter galaxies suggest that their star formation is most intensive in very compact central regions of $\lesssim$1 kpc (e.g., Walter et al. 2009; Riechers et al. 2013; Ikarashi et al. 2015; Venemans et al. 2017b). The water line emission is usually associated with these central regions (Bradford et al. 2011; Riechers et al. 2013). The water emission of PSO145+19N might also indicate intensive star formation within the dense gas of PSO145+19N, but on larger spatial scales than typical (greater than a beam size of $\sim$5 kpc). This star formation could be happening in several interacting (proto)galaxies unresolved in our observations, or in the unresolved star-forming cores within a massive gas-rich galaxy.

4.1. CO Excitation and Molecular Gas Mass

The relative fluxes of the CO(6–5) and CO(7–6) lines of PSO145+19 and PSO145+19N ($I_{\rm CO(7-6)}/I_{\rm CO(6-5)} \approx 0.54$ and 0.58, respectively) indicate that their CO SLEDs peak at transitions $J \lesssim 6$. As the flux ratios of PSO145+19 and PSO145+19N are similar, their CO SLEDs are also likely similar. However, compared to the host galaxies of quasars and star-forming galaxies known at $z \lesssim 7$, the molecular gas of PSO145+19 and PSO145+19N appears to be somewhat less excited. The flux ratios between the CO(6–5) and CO(7–6) lines of these $z \lesssim 7$ galaxies are typically $I_{\rm CO(7-6)}/I_{\rm CO(6-5)} \gtrsim 1$ (Riechers et al. 2009, 2013; Strandet et al. 2017; Venemans et al. 2017a). The estimated CO(6–5) and CO(7–6) luminosities of PSO145+19 and PSO145+19N are a few times higher than those of optically luminous $z > 6$ quasars (Riechers et al. 2009; Wang et al. 2010; Venemans et al. 2017a), but comparable to the luminosities of some massive star-forming galaxies at $z > 6$ (Riechers et al. 2013; Strandet et al. 2017).

The mass of molecular gas is related to CO luminosity as $M_{\rm H2} = \alpha L'_{\rm CO(1-0)}$, where α is the conversion factor (Solomon & Vanden Bout 2005). We estimated the CO(1–0) luminosities of PSO145+19 and PSO145+19N using the CO SLEDs of known sources with the relative fluxes between transitions CO(7–6) and CO(6–5) similar to those of PSO145+19 and PSO145+19N. Among the well-studied star-forming galaxies,

[1] https://catalogs.mast.stsci.edu/

the excitation conditions of molecular gas of PSO145+19 and PSO145+19N might be similar to those of the submillimeter galaxy SMM J16359+6612 at $z = 2.527$ with $I_{CO(7-6)}/I_{CO(6-5)} = 0.49$ (Kneib et al. 2005; Weiß et al. 2005) and the quasar IRAS F10214+4724 at $z = 2.286$ with $I_{CO(7-6)}/I_{CO(6-5)} = 0.77$ (Ao et al. 2008; Riechers et al. 2011). For SMM J16359+6612, the luminosity ratios between the CO(6–5), CO(7–6), and CO(1–0) transitions are $L'_{CO(6-5)}/L'_{CO(1-0)} \approx 0.37$ and $L'_{CO(7-6)}/L'_{CO(1-0)} \approx 0.13$ (Weiß et al. 2005). For IRAS F10214+4724, these ratios are $L'_{CO(6-5)}/L'_{CO(1-0)} \approx 0.52$ and $L'_{CO(7-6)}/L'_{CO(1-0)} \approx 0.29$. Using these relations, the CO(1–0) luminosities of PSO145+19 and PSO145+19N were estimated as the weighted means of the CO(1–0) luminosities independently derived from the CO(6–5) and CO(7–6) lines.

The CO(1–0) flux of high-redshift galaxies is usually converted into the mass of molecular gas using a conversion factor of $\alpha = 0.8\,M_{\odot}(\mathrm{K\,km\,s^{-1}\,pc^2})^{-1}$ inferred from the observations of nearby star-forming galaxies (Solomon & Vanden Bout 2005). Assuming that the gas-to-mass conversion factor is similar for low- and high-redshift star-forming galaxies, the estimated CO(1–0) luminosities of PSO145+19 and PSO145+19N imply that they contain on the order of $10^{11}\,M_{\odot}$ of molecular hydrogen (Table 1). The gas masses of PSO145+19 and PSO145+19N derived using the CO SLEDs of SMM J16359+6612 and IRAS F10214+4724 are comparable. The differences in the gas masses using these two comparison SLEDs reflect the uncertainties related to the unknown shape of the CO SLEDs of PSO145+19 and PSO145+19N. However, both estimates indicate the large masses of the molecular gas of PSO145+19 and PSO145+19N and place them among the largest reservoirs of molecular gas currently known at high redshift. For comparison, the previously reported gas masses of the host galaxies of high-redshift quasars and massive star-forming galaxies are typically on the order of 10^{10}–$10^{11}\,M_{\odot}$ (Wang et al. 2010; Riechers et al. 2013; Strandet et al. 2017; Venemans et al. 2017a).

4.2. Spatial Extent and Dynamical Mass

The characteristic sizes (radii) of the CO(6–5) emission of PSO145+19 and PSO145+19N are ∼4 and 6 kpc. We estimated the dynamical masses of PSO145+19 and PSO145+19N using the isotropic virial estimator with $M_{\mathrm{dyn}} = 2.8 \times 10^5(\mathrm{FWHM})^2 R$, where the FWHM is the CO(6–5) line widths and R is the radius of the CO(6–5) emission in kpc (Binney & Tremaine 2008; Bothwell et al. 2013; Riechers et al. 2013; see Table 1). Thus, molecular gas might constitute more than 45% and 30% of the dynamical masses of PSO145+19 and PSO145+19N, respectively.

The discovered system might be of particular interest for studying physical conditions of star-forming molecular gas at early evolutionary stages of galaxy formation. Further, deeper observations in the near-infrared/submillimeter wavelengths are needed to strengthen the results reported here.

This work was supported by the Ministry of Science and Technology of Taiwan, grant Nos. MOST105-2119-M-007-022-MY3 and MOST107-2119-M-008-009-MY3. Based on data obtained with ALMA (Program 2015.1.01452.S). ALMA is a partnership of ESO (representing its member states), NSF (USA) and NINS (Japan), together with NRC (Canada), *MOST* and ASIAA (Taiwan), and KASI (Republic of Korea), in cooperation with the Republic of Chile. The Joint ALMA Observatory is operated by ESO, AUI/NRAO and NAOJ. Based on observations (Program GN-2017B-DD-4) obtained at the Gemini Observatory, which is operated by the Association of Universities for Research in Astronomy, Inc., under a cooperative agreement with the NSF on behalf of the Gemini partnership: the National Science Foundation (United States), the National Research Council (Canada), CONICYT (Chile), Ministerio de Ciencia, Tecnología e Innovació Productiva (Argentina), and Ministério da Ciencia, Tecnologia e Inovacão (Brazil).

ORCID iDs

Ekaterina Koptelova https://orcid.org/0000-0002-7477-0206
Chorng-Yuan Hwang https://orcid.org/0000-0002-3658-0903

References

Ao, Y., Weiß, A., Downes, D., et al. 2008, A&A, 491, 747
Barnett, R., Warren, S. J., Becker, G. D., et al. 2017, A&A, 601, A16
Becker, G. D., Bolton, J. S., Madau, P., et al. 2015, MNRAS, 447, 3402
Bertoldi, F., Cox, P., Neri, R., et al. 2003, A&A, 409, L47
Binney, J., & Tremaine, S. 2008, Galactic Dynamics (2nd ed.; Princeton, NJ: Princeton Univ. Press)
Blackburne, J. A., Pooley, D., Rappaport, S., et al. 2011, ApJ, 729, 34
Bothwell, M. S., Smail, I., Chapman, S. C., et al. 2013, MNRAS, 429, 3047
Bradford, C. M., Bolatto, A. D., Maloney, P. R., et al. 2011, ApJL, 741, L37
Carilli, C. L., & Walter, F. 2013, ARA&A, 51, 105
Chambers, K. C., Magnier, E. A., Metcalfe, N., et al. 2016, arXiv:1612.05560
Fan, L., Knudsen, K. K., Fogasy, J., et al. 2018, ApJL, 856, L5
Fudamoto, Y., Ivison, R. J., Oteo, I., et al. 2017, MNRAS, 472, 2028
Genzel, R., Tacconi, L. J., Gracia-Carpio, J., et al. 2010, MNRAS, 407, 2091
Gray, M. D., Baudry, A., Richards, A. M. S., et al. 2016, MNRAS, 456, 374
Hook, I. M., Jørgensen, I., Allington-Smith, J. R., et al. 2004, PASP, 116, 425
Ikarashi, S., Ivison, R. J., Caputi, K. I., et al. 2015, ApJ, 810, 133
Kneib, J.-P., Neri, R., Smail, I., et al. 2005, A&A, 434, 819
Koptelova, E., Hwang, C.-Y., Malkan, M. A., et al. 2019, ApJ, in press (arXiv:1907.07458)
Koptelova, E., Hwang, C.-Y., Yu, P.-C., et al. 2017, NatSR, 7, 41617
Matsuoka, Y., Onoue, M., Kashikawa, N., et al. 2018, PASJ, 70, S35
Mazzucchelli, C., Bañados, E., Venemans, B. P., et al. 2017, ApJ, 849, 91
McMullin, J. P., Waters, B., Schiebel, D., et al. 2007, in ASP Conf. Ser. 376, Astronomical Data Analysis Software and Systems XVI , ed. R. A. Shaw, F. Hill, & D. J. Bell (San Francisco, CA: ASP), 127
Riechers, D. A., Bradford, C. M., Clements, D. L., et al. 2013, Natur, 496, 329
Riechers, D. A., Carilli, C. L., Maddalena, R. J., et al. 2011, ApJL, 739, L32
Riechers, D. A., Walter, F., Bertoldi, F., et al. 2009, ApJ, 703, 1338
Riechers, D. A., Walter, F., Carilli, C. L., et al. 2006, ApJ, 650, 604
Salomé, P., Guélin, M., Downes, D., et al. 2012, A&A, 545, A57
Solomon, P. M., & Vanden Bout, P. A. 2005, ARA&A, 43, 677
Strandet, M. L., Weiss, A., De Breuck, C., et al. 2017, ApJL, 842, L15
Strandet, M. L., Weiss, A., Vieira, J. D., et al. 2016, ApJ, 822, 80
Venemans, B. P., Walter, F., Decarli, R., et al. 2017a, ApJ, 845, 154
Venemans, B. P., Walter, F., Decarli, R., et al. 2017b, ApJ, 837, 146
Venemans, B. P., Walter, F., Zschaechner, L., et al. 2016, ApJ, 816, 37
Vieira, J. D., Marrone, D. P., Chapman, S. C., et al. 2013, Natur, 495, 344
Walter, F., Bertoldi, F., Carilli, C., et al. 2003, Natur, 424, 406
Walter, F., Carilli, C., Bertoldi, F., et al. 2004, ApJL, 615, L17
Walter, F., Riechers, D., Cox, P., et al. 2009, Natur, 457, 699
Wang, R, Carilli, C. L., Neri, R., et al. 2010, ApJ, 714, 699
Wang, R., Wagg, J., Carilli, C. L., et al. 2011a, ApJL, 739, L34
Wang, R., Wagg, J., Carilli, C. L., et al. 2011b, AJ, 142, 101
Weiß, A., De Breuck, C., Marrone, D. P., et al. 2013, ApJ, 767, 88
Weiß, A., Downes, D., Neri, R., et al. 2007, A&A, 467, 955
Weiß, A., Downes, D., Walter, F., et al. 2005, A&A, 440, L45
Young, J. S., & Scoville, N. Z. 1991, ARA&A, 29, 581